Supplementary Material for: Witnessing Nonequilibrium Entanglement Dynamics in a Quenched Quantum Chain

Denitsa R. Baykusheva,[1] Mona H. Kalthoff,[2] Damian Hofmann,[2] Martin Claassen,[3] Dante M. Kennes,[4,2] Michael A. Sentef,[2] and Matteo Mitrano[1]

[1] *Department of Physics, Harvard University, Cambridge, Massachusetts 02138, USA*
[2] *Max Planck Institute for the Structure and Dynamics of Matter, Center for Free-Electron Laser Science (CFEL), Luruper Chaussee 149, 22761 Hamburg, Germany*
[3] *Department of Physics and Astronomy, University of Pennsylvania, Philadelphia, PA 19104, USA*
[4] *Institut für Theorie der Statistischen Physik, RWTH Aachen University, 52056 Aachen, Germany and JARA-Fundamentals of Future Information Technology, 52056 Aachen, Germany*

(Dated: January 12, 2023)

S1. MODEL SYSTEM

In this work, we map a half-filled chain of spinless fermions interacting through nearest neighbor Coulomb repulsion onto a corresponding spin Hamiltonian. The initial model Hamiltonian is given by:

$$\hat{\mathcal{H}}(t) = -\frac{J}{2}\sum_j (\hat{c}_j^\dagger \hat{c}_{j+1} + \text{H.c.}) + V(t)\sum_j \tilde{n}_j \tilde{n}_{j+1}, \tag{1}$$

where $\hat{c}_j^\dagger$ ($\hat{c}_j$) is a fermionic creation (annihilation) operator at site j, $\tilde{n}_j = \hat{c}_j^\dagger \hat{c}_j - 1/2$ is the number operator relative to half filling, J is a constant hopping amplitude, and $V(t)$ is a time-dependent, nearest-neighbor Coulomb interaction. Through the Jordan-Wigner transformation [1], this charge Hamiltonian maps onto an equivalent spin-1/2 anisotropic Heisenberg (XXZ) chain (Fig. 1a in the main text):

$$\hat{\mathcal{H}}_{\text{sp}}(t) = \sum_j \left[-\frac{J}{2}\left(\hat{S}_j^+ \hat{S}_{j+1}^- + \text{H.c.}\right) + V(t)\hat{S}_j^z \hat{S}_{j+1}^z \right], \tag{2}$$

where $\hat{S}_j^\pm = \frac{1}{2}\left(\hat{S}_j^x \pm \hat{S}_j^y\right)$ and $\hat{S}_j^\alpha$ ($\alpha = x, y, z$) are the usual spin operators defined in terms of the Pauli matrices $\hat{S}^\alpha = \frac{1}{2}\hat{\sigma}_\alpha$. In this picture, the hopping amplitude J becomes the exchange coupling while $\Delta(t) = V(t)/J$ quantifies the anisotropy of the spin interactions.

At equilibrium, this dual quantum chain exhibits well-known quantum phase transitions. Upon increasing $\Delta = V/J$, the fermionic chain evolves from a gapless Luttinger liquid (LL) phase with short-range correlations to a charge density wave (CDW) phase with long-range correlations. The XXZ chain instead undergoes two separate transitions into an Ising ferromagnet ($\Delta < -1$) and antiferromagnet ($\Delta > 1$), while for ($|\Delta| < 1$) it exhibits an XY phase [1]. Since the dual charge and spin formulations are one-to-one equivalent, we choose to study the time-dependent dynamics of the quantum spin chain using exact diagonalization (ED). The ED calculations for finite-size chains extending up to $L = 24$ sites are performed using the QuSpin [2, 3] as well as the HPhi [4] packages. The antiferromagnetic XXZ ground state in a finite-size system contains a mixture of nearly-degenerate states (notably $|\uparrow\downarrow \ldots \uparrow\downarrow\rangle \pm |\downarrow\uparrow \ldots \downarrow\uparrow\rangle$). In order to break this near degeneracy, which turns into complete degeneracy in the thermodynamic limit, we also introduce a small staggered magnetic field $\hat{\mathcal{H}}_{\text{ext}} = \sum_j (-1)^j h_z \hat{S}_j^z$ to select a specific spin configuration (cf. next section). This ensures that the disconnected part of the spin correlation function in Eq. (2) in the main text vanishes in the limit $\Delta \to \infty$. Our spin sector quench dynamics is then benchmarked for selected conditions against real-time density matrix renormalization group (DMRG) calculations [5] of the time evolution of an infinite chain.

S2. FINITE-SIZE EFFECTS ON THE QUANTUM FISHER INFORMATION CALCULATIONS

In the antiferromagnetic (AFM) Ising limit $\Delta \to \infty$, the ground state of the XXZ chain in the spin sector is degenerate in the thermodynamic limit ($L \to \infty$) and is given by the two possible Néel states $|\uparrow\downarrow\uparrow\downarrow \ldots\rangle$ and $|\downarrow\uparrow\downarrow\uparrow \ldots\rangle$, related to each other via a site translation. At finite L, the two lowest-energy spin configurations $|\uparrow\downarrow\uparrow\downarrow \ldots\rangle \pm |\downarrow\uparrow\downarrow\uparrow \ldots\rangle$ are split by a finite energy gap that decreases as $\propto e^{-\alpha L}$ with increasing system size (with $\alpha > 0$). For the AFM ground state at finite L, the disconnected part of the spin correlation function in Eq. (2) of the main text, i.e. $\sum_{l,k}(-1)^{l+k}\left\langle \hat{S}_l^z \right\rangle \left\langle \hat{S}_k^z \right\rangle$, vanishes, leading to an asymptotically finite value of the QFI F_Q. In order to reinstate

the proper behaviour of the QFI certified by the DMRG calculations in the charge sector, we introduce a staggered degeneracy-breaking magnetic field term $\hat{\mathcal{H}}_{\rm ext} = \sum_j (-1)^j h_z \hat{S}^z_j$ to select a specific Néel component of the ground state and restore the proper limit of F_Q. Consequently, the position of the maximum of the equilibrium QFI density shown in Fig. 1b of the main text thus becomes dependent on the magnitude h_z of this additional term. In addition, both the magnitude of the QFI maximum as well as its position are dependent on the chain length L. In Fig. S1, we plot the equilibrium QFI density in the spin sector as a function of the staggered magnetic field for a fixed chain length (panel a) and as a function of the system size for a fixed h_z.

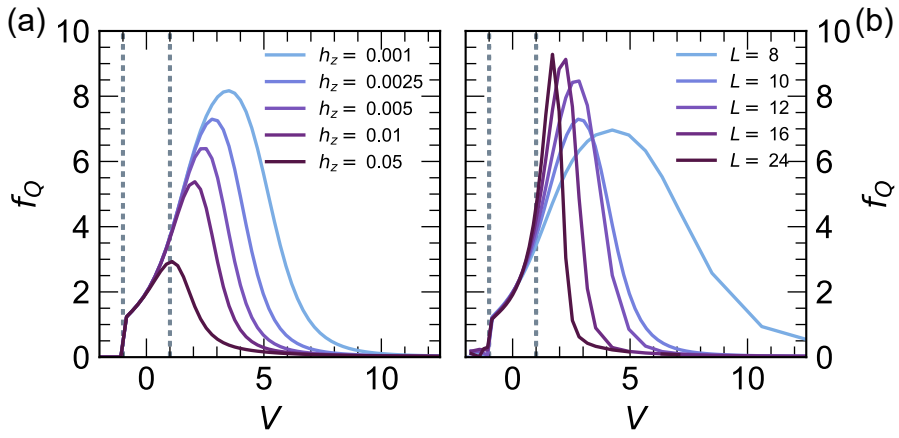

FIG. S1. (a) Equilibrium QFI density f_Q for a spin chain with $L = 10$ for different values of the staggered magnetic field h_z. (b) QFI density as a function of the chain length for a fixed $h_z = 1.414$.

S3. TIME-FREQUENCY ANALYSIS OF THE NON-EQUILIBRIUM QFI

In Fig. 2 of the main text and the accompanying discussion, we outline the main features of the nonequilibrium QFI dynamics. Upon crossing the critical point $\Delta = 1$, the driven system passes through a more entangled state compared to the initial condition. Depending on the ramp velocity, the QFI density $f_Q(t) = F_Q(t)/L$ either maps onto the equilibrium phase diagram, thereby decaying asymptotically to zero as $t \to \infty$, or exhibits a rich oscillatory behaviour when the driving protocol reaches the impulsive limit at sufficiently high velocities. In this section, we focus on origin of the oscillatory dynamics, while the transition between adiabatic and impulsive regimes is discussed in Sec. S5.

We start by focusing our attention on the 1D linecuts of $f_Q(t)$ plotted in Fig. 2c of the main text. In panel a of Fig. S2, we present three of these curves as a function of physical time instead of the time-dependent nearest-neighbour Coulomb repulsion $V(t)$. Both representations are related through the transformation $t = V(t)/v$. The time-domain representation allows us to better appreciate characteristic dynamical features of the non-adiabatic regime ($v > 3.5$). First, all curves in Fig. S2a reveal a slow oscillation at $\nu_{\rm osc} \sim 0.36$, independent of the driving speed. Furthermore, all curves also contain very fast oscillations, evident at early times and featuring a pronounced chirp. In order to isolate the different frequency contributions and characterize the change of the non-stationary contributions as a function of time, we perform a short-time Fourier transform (STFT) analysis. In the resulting spectrogram, a stationary frequency manifests itself as a horizontal line, whereas a linear change of the frequency over time corresponds to a linear chirp.

In panels b-d of Fig. S2, we plot the spectrograms corresponding to the three velocities $v = 2.0$, $v = 10.0$, and $v = 40.0$. The v-independent oscillations correspond to the low-frequency mode at $\nu_{\rm osc} \sim 2\pi\Delta_{01} \approx 0.36$. The fast oscillations show a linear chirp, which emerges outside of the adiabatic limit, with a slope given by $\bar{b} \sim \frac{v}{2\pi}$.

We now discuss the microscopic origin of these features with the aid of Fig. S3. By analyzing the energy level diagram of the $L = 10$ chain (with h_z fixed at 0.005), we can attribute the $\nu_{\rm osc} \sim 0.36$ oscillation to a transition between the ground and the first excited level. The corresponding energy separation Δ_{01} is shown as a function of the nearest-neighbour Coulomb repulsion for different chain sized in Fig. S3a. For $L = 10$ and sufficiently large

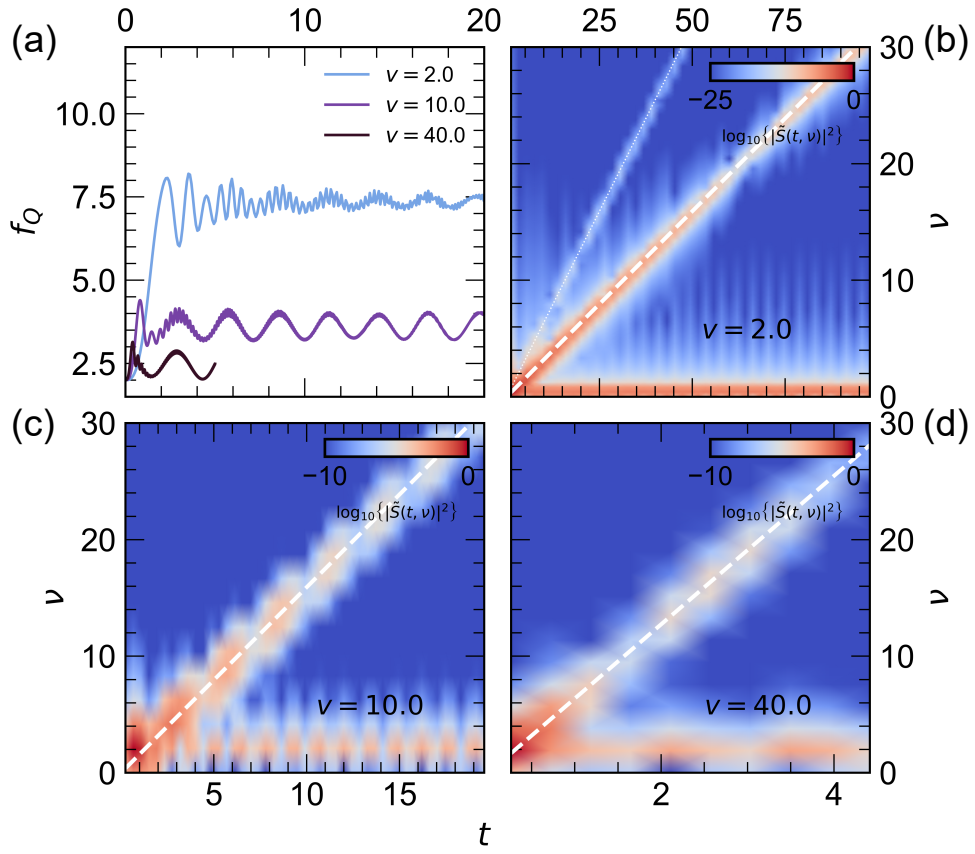

FIG. S2. (a) Linecuts from Fig. 2c in the main text, plotted as a function of time. (b) - (d) spectrograms of the time-dependent QFI density for three selected velocities: $v = 2$ (b), $v = 10$ (c), and $v = 40$ (d). Note that the color scale is logarithmic. Thick dashed lines indicate the dominant chirp mode $\bar{b} \sim \frac{v}{2\pi}$, while a thin dotted line indicates a second chirp mode with a slope of $2\bar{b}$ for $v = 2$.

anisotropies ($\Delta > 3$), the gap size assumes an asymtoptic value of $\frac{0.314}{2\pi}$, hence, the oscillation frequency in the spectrograms in Fig. S2 is largely time-independent.

The second dominant feature, the linearly-chirped rapid oscillations, has its origin in a transition between the ground state and one of the higher-lying excited levels ($j = 5$). The corresponding gap Δ_{05} increases linearly with V (see Fig. S3b), its slope for $L = 10$ matches well the slope of the corresponding feature in the short-time Fourier transform. The relationship between the two is $\frac{\bar{b}}{v} \sim \frac{1}{2\pi}\frac{\mathrm{d}\Delta_{05}}{\mathrm{d}V}$. The excitation to this (and others) specific state(s) occurs while driving the system through the critical point $\Delta = 1$. In panel c of Fig. S3, we plot the projection of the time-evolved initial pure state $\psi_0(t)$ (coinciding with the GS of the LL-model at $t_0 = 0$) onto the j^{th}-eigenstate of the time-dependent Hamiltonian $\hat{\mathcal{H}}(t)$ (denoted by $\psi_t^{(j)}$) at the *end of the time evolution* $t_{\max}$. Apart from the nearly-degenerate low-lying states with $j = 1, 2$, only the state with $j = 5$ has a significant contribution, and beatings with the $\psi_0(t)$ dominate the time-frequency structure of the non-equilibrium QFI. The state $\psi_t^{(j=5)}$ is dominated by spin configurations featuring two domain walls (e.g. $|\uparrow\uparrow\downarrow\uparrow\uparrow\downarrow\uparrow\downarrow\uparrow\downarrow\rangle$) for all values of t, whereas the time-evolved $\psi_0(t)$, especially after crossing $\Delta = 1$, becomes progressively dominated by the defect-free two Nèel configurations. The projection of $\psi_0(t)$ onto the initial state at t_0, plotted as a dark purple line in Fig. S3c, exhibits an interesting dynamics consisting of a decay followed by multiple revivals. For completeness, in panel d of the same figure we show the temporal evolution of several matrix elements $b_{ij} = \left\langle \psi_t^{(i)} \right| \left|\psi_0(t)\right\rangle \left\langle \psi_0(t)\right| \left|\psi_t^{(j)}\right\rangle$, i.e. the projection of $\psi_0(t)$ over the instantaneous eigenstate at each t. These results imply that the non-equilibrium QFI in the impulsive regime is determined by the non-adiabatic excitation of multiple states at the critical point and the associated increased domain wall density.

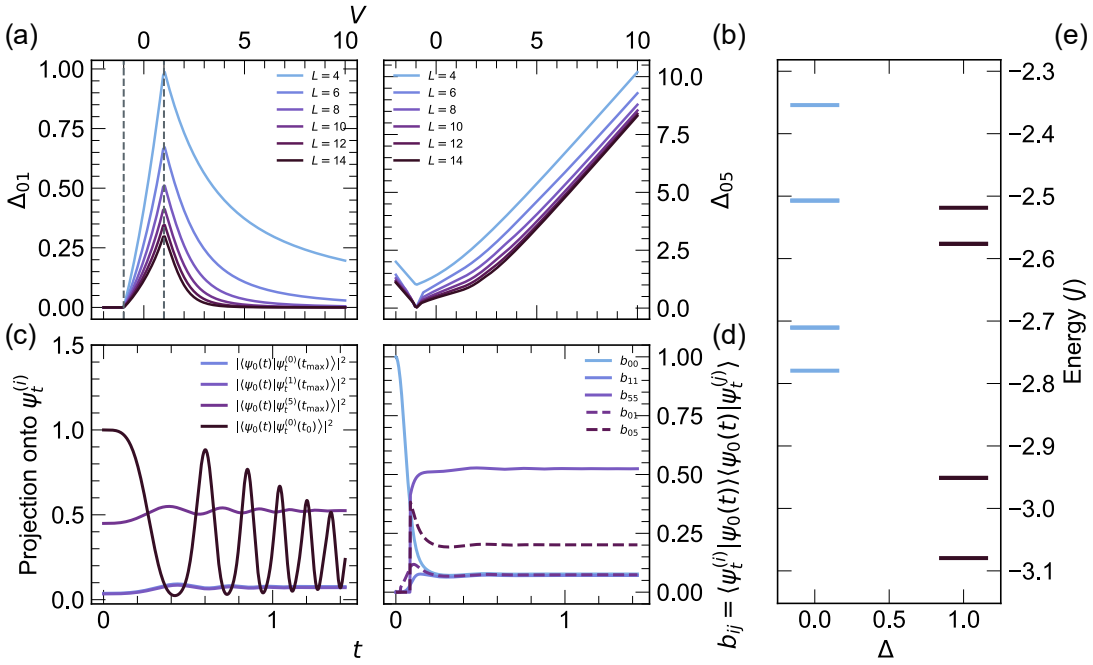

FIG. S3. (a)-(b) Energy separations between the ground state and the first (a) resp. the fifth (b) excited states of the chain, plotted as a function of the nearest-neighbour Coulomb repulsion for different chain lengths. A staggered magnetic field value of $h_z = 0.005$ has been used. Grey vertical lines in (a) indicate the positions of the critical points. (c) Projection of the time-evolved state $\psi_0(t)$ onto selected eigenstates of the *time-dependent* Hamiltonian at the end of the time-evolution $\hat{\mathcal{H}}(t = t_{\max})$. The dark-purple curve shows the projection of ψ_0 onto the initial state at t_0. Panel (d) Time-dependence of selected matrix elements b_{ij}, given by products of overlaps of the time-propagated $\psi_0(t)$ with the eigenstates of the *instantaneous* Hamiltonian $\hat{\mathcal{H}}(t)$ at time t. Panel (e) energy diagram showing the relevant energy levels dominating the dynamics. Some of the energy levels are degenerate.

S4. LINDBLAD MASTER EQUATION

In Fig. S4, we present calculation results showcasing the influence of the decoherence rate on the QFI during non-unitary time evolution ($L = 10$, $h_z = 0.005$). The main non-equilibrium QFI features, i.e. the broad QFI maximum and the subsequent oscillatory dynamics, are preserved for coupling strengths up to $\gamma \sim 0.1$, and progressively fade when $\gamma > 0.1$. The dissipative Lindblad jump operator acting on each site l is given by $\hat{\mathcal{L}}^{(l)} \equiv \hat{\mathcal{L}}_z = \hat{\sigma}_l^z$.

The QFI in the presence of decoherence is calculated by first propagating the density matrix $\hat{\rho}(t)$ obeying the initial condition:

$$\hat{\rho}(t_0) = |\psi_0(t_0)\rangle \langle\psi_0(t_0)| \,. \tag{3}$$

The QFI is obtained as [6]:

$$\mathcal{F}_Q(t) = 2 \sum_{i,j} \frac{\left(\epsilon_t^i - \epsilon_t^j\right)^2}{\epsilon_t^i + \epsilon_t^j} \left|\langle\varphi_t^i| \hat{\mathcal{O}}_\pi |\varphi_t^j\rangle\right|^2 , \tag{4}$$

where ϵ_t^i and $|\varphi_t^i\rangle$ are the eigenvalues and the eigenvectors of $\hat{\rho}$ at time t.

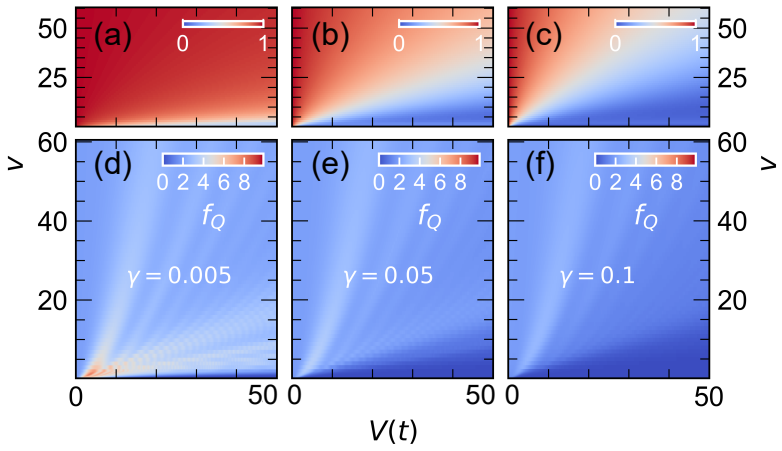

FIG. S4. (a)-(c) Density matrix purity as a function of effective nearest-neighbour Coulomb repulsion and ramp speed. The decoherence rate is set to $\gamma = 0.005$ in panels (a)/(d), to $\gamma = 0.05$ in (b)/(e), and to $\gamma = 0.1$ in (c)/(f). (d)-(f) Non-equilibrium QFI in the presence of decoherence for three different decoherence rates γ, displayed as a function of the effective nearest-neighbour Coulomb repulsion and ramp speed. The colormap is normalized with respect to the unitary QFI density, shown in Fig. 2a of the main text.

S5. KIBBLE-ZUREK ANALYSIS OF THE NONEQUILIBRIUM QFI

The nonequilibrium QFI dynamics (see. Fig. 2a of the main text) of the spinless fermion chain subject to a linear ramp can be broadly divided into three regions depending on the ramp velocity. These regimes can be delineated by tracking the time (t^*) or the effective nearest-neighbour Coulomb interaction ($V(t^*)$) which maximize the time-dependent f_Q at a given ramp speed v. The resulting curve (s. white line in Fig. 2a or Fig. S5a-c) effectively tracks the position of the main QFI "crest" as it propagates towards larger $V(t^*)$ (smaller t^*) on increasing the ramp speed. The positions of the maxima are extracted by fitting a skewed Voigt distribution to the time profile of f_Q at each velocity in a region centered around the main peak.

The two limiting cases are defined by the adiabatic ($v < 0.03$, cf. Fig. S5a) and the nonadiabatic ($v > 3.5$, cf. Fig. S5b-c) limits, separated by an intermediate region. Whereas the onset of the non-adiabatic region is rather sudden and well-marked by a "kink" in the $v - V(t^*)$ resp. $v - t^*$ plots in Fig. S5b-c, the separation between adiabatic and intermediate regions is rather fluid. In the deep adiabatic regime, the position of the f_Q-maximum is weakly dependent on the driving speed, and the driven system essentially traces out the equilibrium phase diagram. This regime (illustrated for $v = 0.001$ in Fig. S5d) holds as long as excitations to the first excited state on crossing the critical point $\Delta = 1$ can be neglected, i.e. $b_{ij} \approx \delta_{0,i}\delta_{0,j}$ for the entire time evolution. Examining the time-resolved data underlying Fig. 2a, we estimate a value of $v^{*,1} \sim 0.03$ for the maximum ramp speed that warrants purely adiabatic evolution before oscillations due to excitations to the first excited state develop. Invoking simple Landau-Zener (LZ) arguments, we can estimate the corresponding excitation probability to the first excited state as $P_{01} = 1 - e^{-\frac{\pi\tilde{\delta}\Delta_{01}^2}{2v}}$, where $\tilde{\delta}$ is a constant related to the rate of change of the gap at $\Delta = 1$ as a function of the critical parameter $V(t)$. The threshold for the breakdown of adiabaticity in the LZ picture ($\Delta_{01}^2 \approx v|\mathrm{d}\Delta_{01}/\mathrm{d}V|$), however, largely overestimates $v^{*,1}$, indicating a more complex behaviour.

For ramp velocities above $v^{*,1}$ but not exceeding $v^{*,2}$, the dynamics falls into the intermediate regime, characterized by an extensive scaling of the QFI density $f_Q \sim L$ in the unitary evolution case. Due to the rapidly oscillating and saturating behaviour of f_Q, the corresponding maxima could not be extracted for velocities ranging from 0.175 up to shortly before the onset of the non-adiabatic region $v^{*,2} \sim 3.5$ (cf. square/diamond symbols in Fig. S5b-c). Here, the dynamics are mainly governed by the ground and the first excited states of the system, as one can deduce from the dominant b_{ij}-coefficients in Fig. S5e. Recalling that in the presence of the staggered magnetic field of amplitude h_z the ground state at t_0 is dominated by one of the two Néel configurations, creating excitations across the gap mixes the wavefunction with the state where the other Néel is dominant. The resulting superposition contains these two components with a similar amplitude, hence the growth of the entanglement.

The non-adiabatic regime has a sharply delineated onset, marked by a rapid change of the slopes of $\Delta v/\Delta V(t^*)$

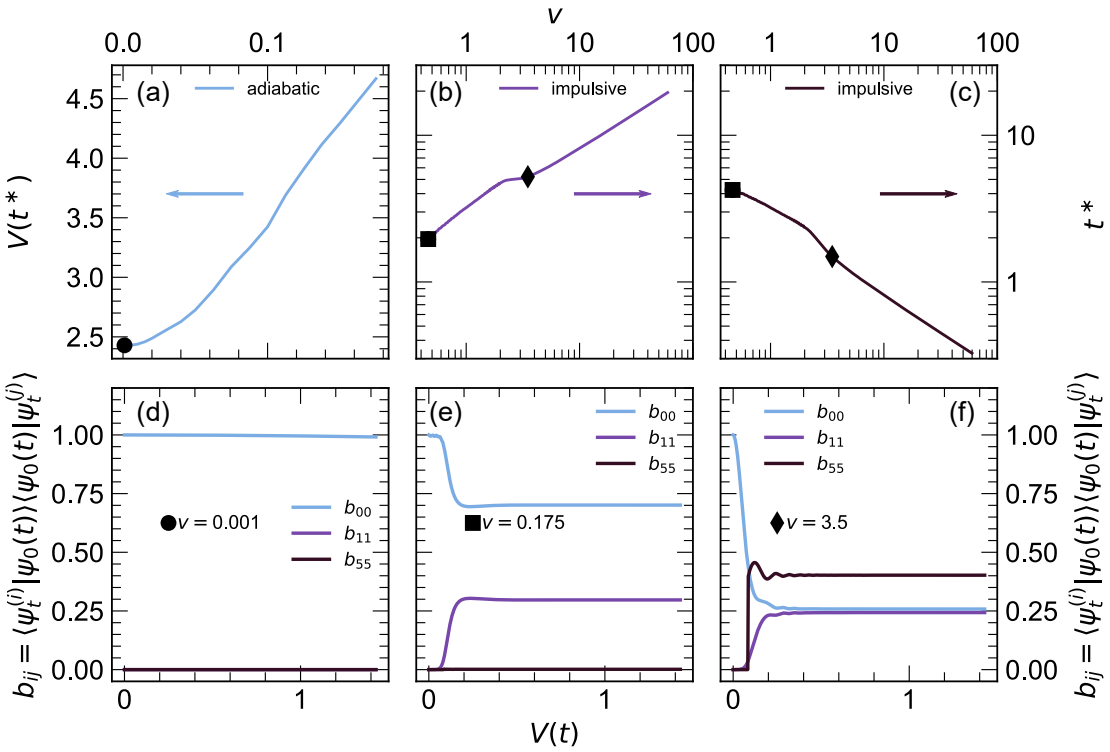

FIG. S5. (a)-(c) Positions of the maxima of the time-dependent QFI density f_Q as a function of the ramp velocity, displayed as a function of the effective nearest-neighbour Coulomb repulsion [panels (a) and (b)] or time (c). Points falling into the adiabatic and (partially) to the "intermediate" regime are shown in panel (a). Panels (b) and (c) show the "intermediate" and the non-adiabatic regions on a double-logarithmic scale. The onset of the non-adiabatic regime is manifested by a marked change in the slope of the curves (see text). The symbols indicate the positions of the three different ramp velocities corresponding to the data in the bottom row. (d)-(f) Time-dependent matrix elements b_{ij}, given by products of overlaps of the time-propagated $\psi_0(t)$ with the eigenstates of the *instantaneous* Hamiltonian $\hat{\mathcal{H}}(t)$ at time t, shown for three different velocities (see legends).

resp. $\Delta v/\Delta t^*$. The nonadiabatic limit commences when the probability of an excitation to the higher-lying states (in particular $j = 5$ for the $L = 10$ chain) exceeds the corresponding excitation fraction to the first excited state $j = 1$ (cf. Fig. S5f), leading to proliferation of defects. As visible in Fig. S6, the dynamics of the defect proliferation closely follows the dynamical QFI, and we therefore we track the temporal maximum of f_Q as a function of the ramp velocity and interpret the results with the aid of a KZ scaling analysis. In this regime, the maximum of the QFI density follows a regular behaviour, and its functional dependence can be extracted by fitting the corresponding slopes in Fig. S5b-c: $V(t^*) \propto \sqrt{v}$ resp. $t^* \propto v^{-1/2}$. The exact values of the slopes are 0.5295 ± 0.0009 and -0.5937 ± 0.0019, respectively. With the aid of the critical exponents of the system at $\Delta = 1$, we can relate the scaling of the entanglement jet to the corresponding scaling of the density of defects in a Kibble-Zurek type of analysis:

$$d_{\mathrm{KZ}} \propto \frac{a_0}{\xi_0} \left(\tau_0 v\right)^{1/2}, \tag{5}$$

where a_0, ξ_0, τ_0 are the characteristic length scale, correlation length, and relaxation rate of the system. Note that a KZ-analysis has a limited validity at the phase transition at the $\Delta = 1$ critical point is of BKT type instead of a second-order one.

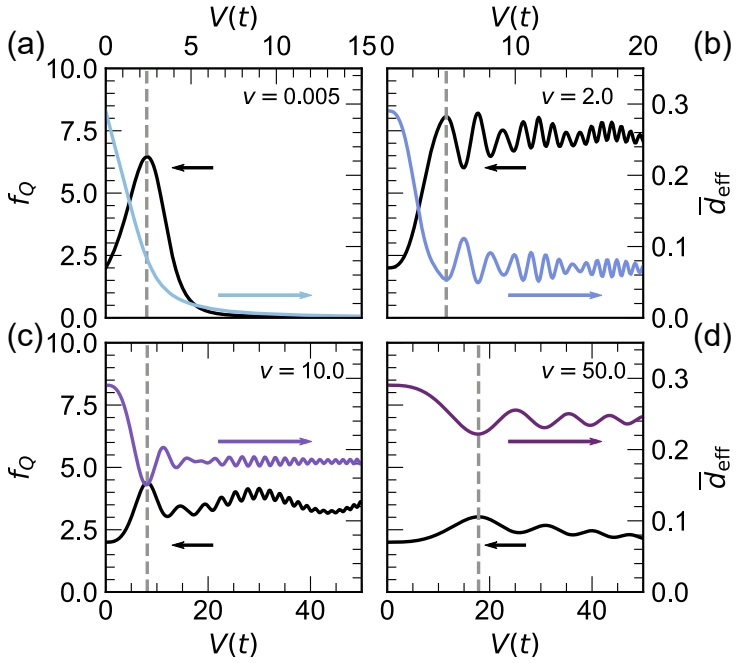

FIG. S6. Relation of the dynamical QFI density to the time evolution of the integrated density of states for four representative ramp velocities: $v = 0.005$ (a), $v = 2.0$ (b), $v = 10.0$ (c), and $v = 50.0$ (d). Each panel shows the integrated density of defects (color) plotted against the corresponding $f_Q(t)$ at that velocity (black).

S6. NONEQUILIBRIUM QFI IN PRESENCE OF NEXT-NEAREST-NEIGHBOR INTERACTIONS

Finally, we corroborate the stability (or universality) of the nonequilibrium QFI features by also considering the role of additional interactions, that break integrability in the infinite system [7]. We specifically study the dynamical QFI for the spinless fermion chain at half-filling (Eq. (1)) with the inclusion of next-nearest-neighbor interactions of the form $\hat{\mathcal{H}}_{(2)} = V^{(2)} \sum_l \tilde{n}_l \tilde{n}_{l+2}$. The results presented in Fig. S7c for a second-order coupling of $V^{(2)} = 2$ illustrate that the main traits of the nonequilibrium QFI dynamics are preserved. Importantly, this observation underscores the generic character and robustness of our main findings and suggests that they should be observable across many different experimental platforms, irrespective of microscopic details.

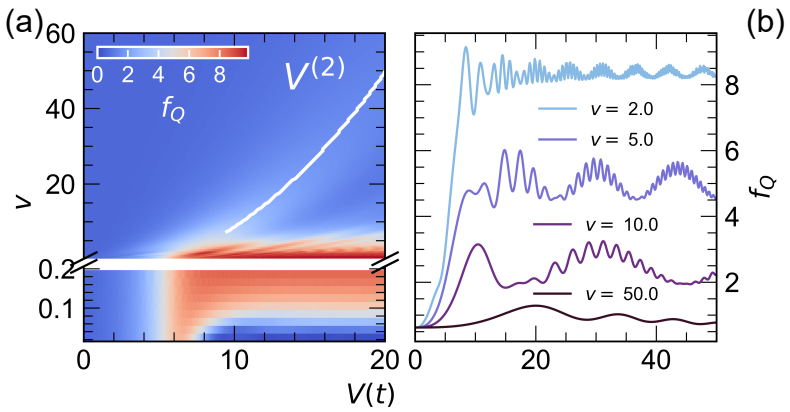

FIG. S7. (a) Non-equilibrium QFI for a Heisenberg chain featuring additional next-nearest neighbour interaction term $\hat{\mathcal{H}}_{(2)}$ as a function of the nearest-neighbour Coulomb repulsion and the ramp speed. (b) Selected 1D line cuts for several ramp velocities.

S7. DYNAMICAL QFI AND ORDER PARAMETER

In this section, we compare the dynamical QFI density to the time evolution of the order parameter of the LL → CDW phase transition, i.e. the staggered magnetization $\mathcal{M}_{\text{stagg}}(t)$. In Fig. S8, we present the dynamical behaviour of $\mathcal{M}_{\text{stagg}}(t)$ for a $L = 10$ chain subject to a time-dependent nearest-neighbor linear interaction ramp $V(t)$ and including a small staggered magnetic field $h_z = 0.005$. We choose four representative ramp velocities spanning the adiabatic, intermediate, and impulsive interaction regimes. The behaviour of the two quantities $f_Q(t)$ and $\mathcal{M}_{\text{stagg}}(t)$ displays qualitative similarities in the intermediate and impulsive regions, but vast discrepancies in the adiabatic limit.

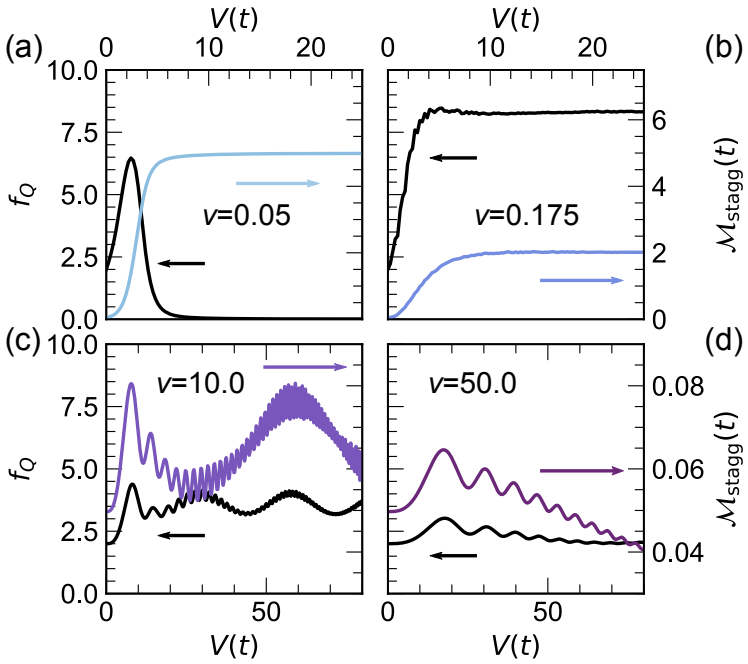

FIG. S8. Relation of the dynamical QFI density to the time evolution of the order parameter of the LL → CDW phase transition for four representative ramp velocities: $v = 0.05$ (a), $v = 0.175$ (b), $v = 10.0$ (c), and $v = 50.0$ (d). Each panel shows the staggered magnetization $\mathcal{M}_{\text{stagg}}(t)$ (color) plotted against the corresponding $f_Q(t)$ at that velocity (black). The calculations are performed for a chain of size $L = 10$ and a staggered magnetic field of $h_z = 0.005$.

Due to the presence of the additional staggered magnetization term h_z, $\mathcal{M}_{\text{stagg}}(t)$ saturates to a finite asymptotic value in the CDW phase and does not exhibit a maximum at the critical point for adiabatic ramps (cp. Fig. S8a). In the absence of an additional staggered magnetic field, $\mathcal{M}_{\text{stagg}}(t)$ evaluates to zero irrespective of the ramp velocity due to the canceling contributions from the degenerate Néel states.

Overall, the staggered magnetization reaches its maximum value for adiabatic ramps. In the intermediate, "critical" region, where f_Q is superextensive ($f_Q \sim L$), $\mathcal{M}_{\text{stagg}}$ saturates at a lower value with respect to the adiabatic case (Fig. S8b). In the impulsive limit (panels c and d), the position of the first QFI crest is mirrored in a maximum in the staggered magnetization. The subsequent fast oscillations of the two quantities are phase-synchronized at first, but slowly go out of phase with progressing time. Furthermore, the periodicity of the slow oscillatory motion is completely different in both cases. More importantly, for fast ramps $v \geq 40$, the staggered magnetization remains very small ($\mathcal{M}_{\text{stagg}} < 0.05$) throughout the entire time evolution. In contrast, the QFI density reaches values exceeding the classical bound for all considered ramp velocities.

S8. QFI DYNAMICS AT FINITE TEMPERATURE

While the numerical results included in the main follow the evolution of a pure initial state, this assumption is rarely fulfilled in macroscopic physical systems, where the starting point is often represented by a mixed state at thermal equilibrium. To demonstrate the validity of our results also in the experimentally-relevant situation of mixed initial states, we have calculated the dynamical evolution of the QFI under a linear interaction ramp starting from

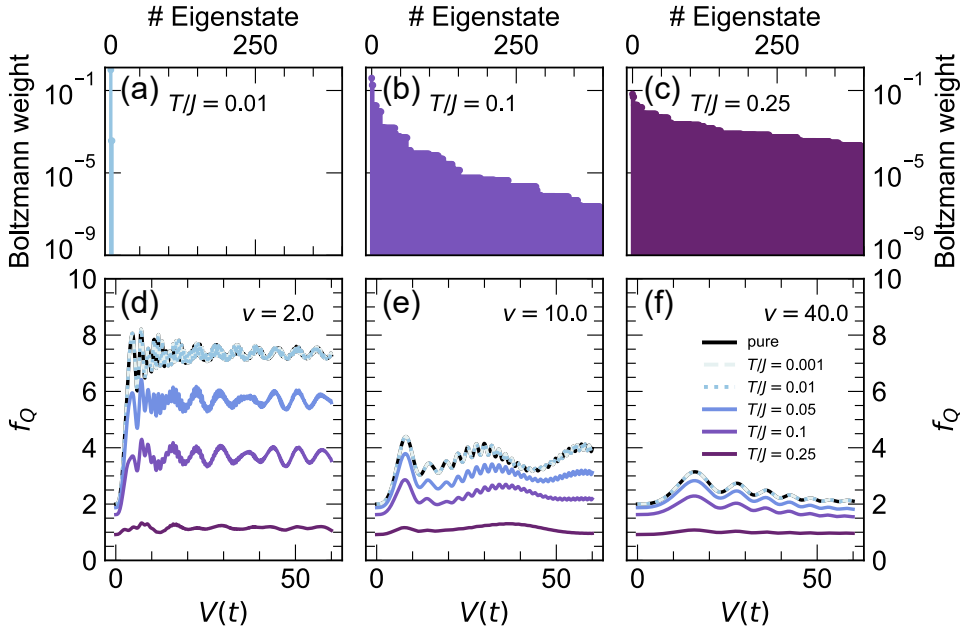

FIG. S9. Non-equilibrium QFI for thermal states at various temperatures. Panels (a), (b), and (c) display the distribution of the Boltzmann factors over the eigenstates of a $L = 10$ spinless fermionic chain for three different temperatures T/J: 0.01, 0.1, and 0.25. Panels (d) - (f) show the non-equilibrium QFI density f_Q for selected temperatures for the following three velocities: $v = 2.0$ (d), $v = 10.0$ (e), and $v = 40.0$ (f). Note that the dynamics at $T/J = 0.001$ and $T/J = 0.01$ follow closely the pure state dynamics such that the three curves are nearly coincident.

a thermal ensemble. In Fig. S9, we present numerical results for the Liouville-von-Neumann evolution of a $L = 10$ spinless fermionic chain subject to a nearest-neighbour Coulomb interaction quench at varying ensemble temperatures (reported in terms of the ratio T/J) and for three representative ramp velocities. From these results, we can deduce the following: first and most important, the main features of the pure-state QFI dynamics, i.e. the initial rise of the system entanglement, the broad maximum, and the subsequent oscillatory structure – are preserved in this mixed-state case, and the initial population of higher-lying states generally reduces the QFI density. For temperatures up to $T/J \sim 0.01$, this decrease is negligible. At higher temperatures (up to $T/J \sim 0.1$), the QFI is increasingly suppressed (while still exceeding the classical bound) and the features of its temporal evolution (such as the phase of the oscillations) are preserved. Above $T/J \sim 0.2$ the QFI decreases below the classical bound, thus preventing its use as a multipartite entanglement witness.

These thermal states are directly relevant to real condensed-matter systems, where the mixed-state QFI can be extracted via an integral of the dynamical susceptibility [6] as measured e.g. in inelastic neutron scattering experiments [8, 9]. Typical values of the exchange constant J for the Mott-insulating model systems considered in this work are on the order of few tenths of eV: e. g., 0.1 eV for $\mathrm{ET-F_2TCNQ}$ [10], 0.17 eV for Sr_2CuO_3 [11], or 0.26 eV for $[\mathrm{Ni\,(chxn)_2\,Br}]\mathrm{Br_2}$ [11]. Given the thermal energy of 0.025 eV, this leads to T/J-values of $0.1 - 0.25$ at room temperature. At cryogenic temperatures (< 30 K), T/J can be suppressed by an order of magnitude. Thus, depending on the exact material, the mixed state QFI for a thermal initial state under experimentally-relevant temperature conditions closely follows the prototypical pure state evolution discussed in the main text.

[1] T. Giamarchi, *Quantum physics in one dimension*, International series of monographs on physics (Clarendon Press, Oxford, 2004).

[2] P. Weinberg and M. Bukov, QuSpin: a Python Package for Dynamics and Exact Diagonalisation of Quantum Many Body Systems. Part I: spin chains, SciPost Phys. **2**, 003 (2017).

[3] P. Weinberg and M. Bukov, QuSpin: a Python Package for Dynamics and Exact Diagonalisation of Quantum Many Body Systems. Part II: bosons, fermions and higher spins, SciPost Phys. **7**, 20 (2019).

[4] M. Kawamura, K. Yoshimi, T. Misawa, Y. Yamaji, S. Todo, and N. Kawashima, Quantum lattice model solver HΦ, Computer Physics Communications **217**, 180 (2017).

[5] D. M. Kennes, A. de la Torre, A. Ron, D. Hsieh, and A. J. Millis, Floquet Engineering in Quantum Chains, Phys. Rev. Lett. **120**, 127601 (2018).
[6] P. Hauke, M. Heyl, L. Tagliacozzo, and P. Zoller, Measuring multipartite entanglement through dynamic susceptibilities, Nature Publishing Group **12**, 778 (2016).
[7] K. Patrick, V. Caudrelier, Z. Papić, and J. K. Pachos, Interaction distance in the extended xxz model, Phys. Rev. B **100**, 235128 (2019).
[8] A. Scheie, P. Laurell, A. M. Samarakoon, B. Lake, S. E. Nagler, G. E. Granroth, S. Okamoto, G. Alvarez, and D. A. Tennant, Witnessing entanglement in quantum magnets using neutron scattering, Phys. Rev. B **103**, 224434 (2021).
[9] P. Laurell, A. Scheie, C. J. Mukherjee, M. M. Koza, M. Enderle, Z. Tylczynski, S. Okamoto, R. Coldea, D. A. Tennant, and G. Alvarez, Quantifying and Controlling Entanglement in the Quantum Magnet Cs_2CoCl_4, Phys. Rev. Lett. **127**, 037201 (2021).
[10] S. Wall, D. Brida, S. R. Clark, H. P. Ehrke, D. Jaksch, A. Ardavan, S. Bonora, H. Uemura, Y. Takahashi, T. Hasegawa, H. Okamoto, G. Cerullo, and A. Cavalleri, Quantum interference between charge excitation paths in a solid-state Mott insulator, Nature Physics **7**, 114 (2011).
[11] S. Iwai, M. Ono, A. Maeda, H. Matsuzaki, H. Kishida, H. Okamoto, and Y. Tokura, Ultrafast Optical Switching to a Metallic State by Photoinduced Mott Transition in a Halogen-Bridged Nickel-Chain Compound, Phys. Rev. Lett. **91**, 057401 (2003).